Chemical Science

ROYAL SOCIETY OF CHEMISTRY

EDGE ARTICLE

View Article Online
View Journal | View Issue

Cite this: *Chem. Sci.*, 2022, **13**, 12180

All publication charges for this article have been paid for by the Royal Society of Chemistry

Received 30th June 2022
Accepted 30th August 2022

DOI: 10.1039/d2sc03659b

rsc.li/chemical-science

Mesoporous multi-shelled hollow resin nanospheres with ultralow thermal conductivity†

Ruilin Yuan,[a] Chun Wang,[a] Long Chen,[a] Han Cheng,[a] Wentuan Bi,[a] Wensheng Yan,[b] Yi Xie[a] and Changzheng Wu *[a]

Hollow nanostructures exhibit enclosed or semi-enclosed spaces inside and the consequent features of restricting molecular motion, which is crucial for intrinsic physicochemical properties. Herein, we developed a new configuration of hollow nanostructures with more than three layers of shells and simultaneously integrated mesopores on every shell. The novel interior configuration expresses the characteristics of periodic interfaces and abundant mesopores. Benefiting from the suppression of gas molecule convection by boundary scattering, the thermal conductivity of mesoporous multi-shelled hollow resin nanospheres reaches 0.013 W m^{-1} K^{-1} at 298 K. The designed interior mesostructural configuration of hollow nanostructures provides an ideal platform to clarify the influence of nanostructure design on intrinsic physicochemical properties and propels the development of hollow nanostructures.

Introduction

Hollow nanostructures arouse extensive research interest because of their attractive physicochemical properties such as low mass density, tunable chemistries, and confined space, which make them competitive candidates in diverse applications.[1,2] To meet the specific needs of different application scenarios, the precise design of the configuration of hollow nanostructures has been extensively required.[3,4] Hollow nanostructures with different interior structures have been developed, such as single- or multi-shelled hollow nanostructures of spheres,[5–8] tubes,[9,10] cubes,[11,12] and their hierarchical nanostructures.[13,14] Among them, mesoporous multi-shelled hollow nanospheres exhibit the unique characteristics of periodic interfaces and abundant mesopores, providing ideal platforms to modulate properties sensitive to molecular motion that is essential for mass transportation.

To obtain mesoporous multi-shelled interior configurations of hollow nanospheres, repetitive synthesis programs or multiple hierarchical templates are usually utilized as effective strategies, which have been implemented in serial material systems such as oxides,[6,8] alloys,[15] and activated carbons.[7,16,17] For example, repeated cycles of programmed reaction temperature or sequential templating approaches have been employed to achieve a number of multi-shelled hollow metal oxides or metal hydroxides, such as VOOH,[5] Nb_2O_5,[6] $ZnFe_2O_4$,[8] *etc.* On the other hand, mesoporous multi-shelled hollow nanostructures of polymers,[16,17] carbon[7] or silica[18,19] are generated, by utilizing surfactant templates with organic cosolvent or dual template systems with different sizes. Despite tremendous efforts to achieve mesoporous multi-shelled hollow nanostructures, concise and facile strategies are urgently expected to reduce the complexity of synthesis and regulation.

Herein, we report a new configuration of hollow nanospheres with more than three layers of mesoporous shells, featuring abundant pores and periodic interfaces. An *in situ* polymerization strategy is developed to construct multi-shelled nanostructures by a single type of soft template, without additional additives and repetitive programs. And mesopores are simultaneously introduced during the pyrolysis removal process of the soft template, simplifying the complex synthesis. The abundant mesopores and periodic interfaces of mesoporous multi-shelled hollow resin nanospheres increase the probability of molecule-boundary scattering and thus limit gas molecular motion. As expected, mesoporous multi-shelled hollow resin nanospheres contribute to ultralow thermal conductivity, which is sensitive to gas molecular motion.

Results and discussion

Synthesis mechanism

In this work, an *in situ* polymerization strategy was utilized to immobilize the multi-shelled morphology of soft template P-123 vesicles. Benefiting from the alkaline medium for melamine/phenol-formaldehyde resin (MPF) synthesis, the hydrophilic EO moieties in P-123 went through deprotonation,

[a]*School of Chemistry and Materials Science, University of Science and Technology of China, Hefei, Anhui, 230026, P. R. China. E-mail: czwu@ustc.edu.cn*

[b]*National Synchrotron Radiation Laboratory, University of Science and Technology of China, Hefei, Anhui, 230029, P. R. China*

† Electronic supplementary information (ESI) available. See https://doi.org/10.1039/d2sc03659b

thus reducing its hydrophilicity. Therefore, the polar head surface area of P-123 decreased, which led to an increase in the packing parameter and the aggregate morphology of P-123 changed to multi-shelled vesicles.[1,20,21] As demonstrated in Fig. 1a, resin monomers are *in situ* polymerized in the hydrophilic region of P-123 vesicles, immobilizing the multi-shelled configuration. With the assistance of the soft template, multi-shelled resin nanospheres with P-123 were successfully synthesized *via* an *in situ* polymerization strategy.

Abundant mesopores and hollow configuration were derived from the removal of the template. The mesoporous structure derived from the gas products escaping from the pyrolysis process of P-123, as gas molecules pass through and slightly etch the resin shells.[22] The process was analyzed by *in situ* thermogravimetry-Fourier transform infrared measurement in detail. The thermogravimetry (TG) curve (Fig. S1†) indicated two stages of mass loss. From room temperature to 573 K, the weight loss of MPF nanospheres with P-123 was about 5%. And the Fourier transform infrared (FT-IR) spectra of evolved gaseous products (Fig. 1b and c) showed that bands corresponding to C=O and CHO firstly appeared at 440 K,[23] which were derived from the escape of incomplete polymerized formaldehyde from MPF. From 573 K to 723 K, MPF with P-123 experienced severe weight loss. This stage was roughly divided into two phases according to FT-IR spectra. Firstly, from 573 K to 673 K, only the spectral bands of alcohols and ethers appeared, which were generated by the decomposition of P-123.[24,25] After the phase of P-123 decomposition, double peaks near 2280 cm^{-1} appeared at 673 K, which indicated that part of the MPF skeleton began to decompose into CO_2.[26] The FT-IR spectrum at 695 K (Fig. 1c) showed that both CO_2 and alcohols were present in the gas products. The TG curves of P-123 and MPF (Fig. S2†) revealed that the temperature corresponding to the maximum decomposition rate of P-123 and MPF nanospheres occurred at 657 K and 710 K respectively, indicating that P-123 decomposes before MPF. In our case, MPF with P-123 was pyrolyzed under H_2-rich argon (denoted as MsH-MPF-H_2) and H_2O-rich argon (denoted as MsH-MPF-H_2O) to

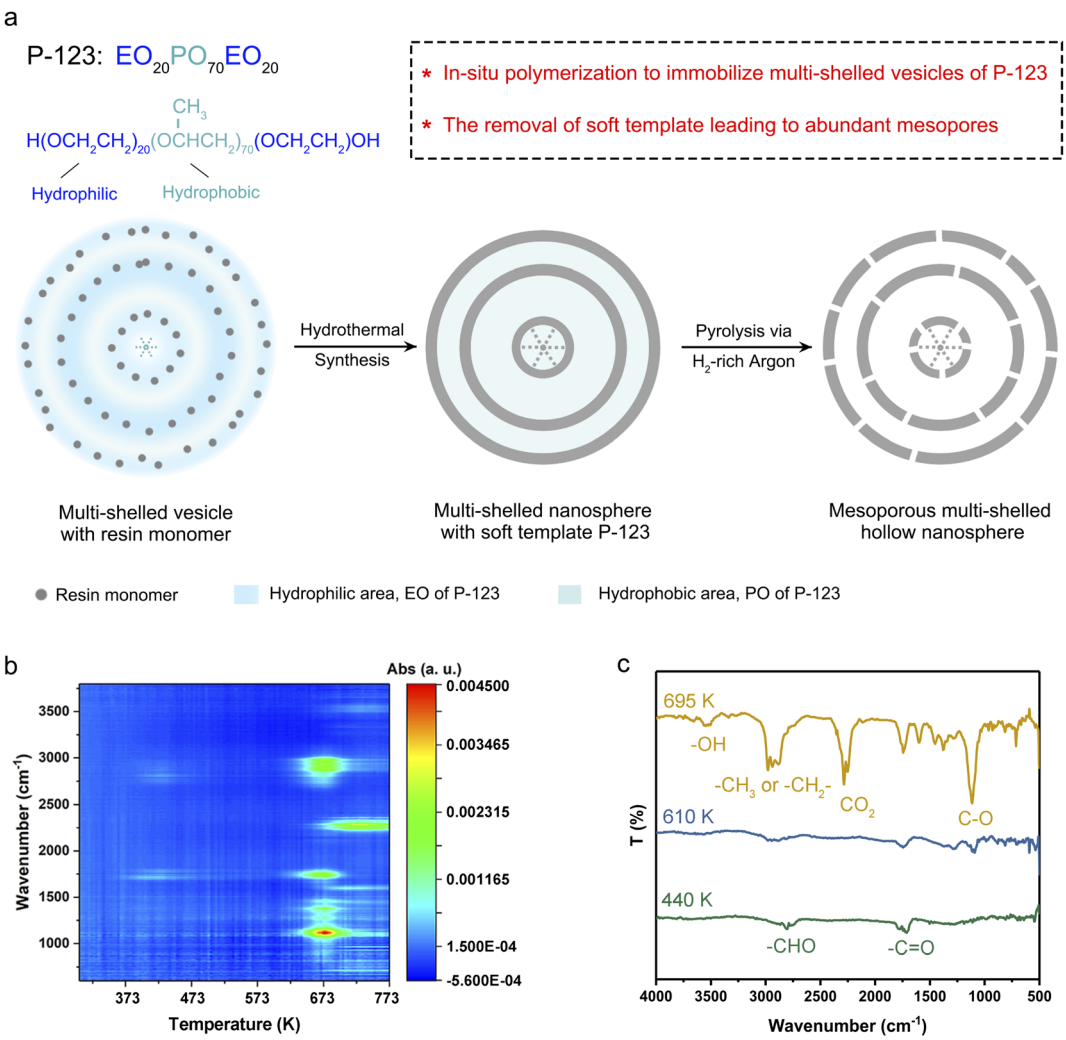

Fig. 1 Synthesis of MsH-MPF-H_2 multi-shelled hollow nanospheres. (a) Schematic illustration of the synthesis program of MsH-MPF-H_2 nanospheres through a template-environment collaboration strategy. (b) Contour diagram of FT-IR spectra for gaseous products of MPF during pyrolysis. (c) FT-IR spectra for gaseous products at different temperatures respectively.

obtain mesoporous multi-shelled hollow resin nanospheres, respectively.

Porosity analysis

The multi-shelled configuration was demonstrated by electron microscopy technologies and small-angle X-ray scattering (SAXS). The transmission electron microscopy (TEM) image of MsH-MPF-H_2 with different magnifications (Fig. 2a and S3†) manifested the multi-shelled hollow nanostructures, similar to that of MsH-MPF-H_2O. The typical four-layer shells and three-layer shells of both MsH-MPF-H_2 and MsH-MPF-H_2O are graphically illustrated in Fig. S3.† The corresponding scanning electron microscopy (SEM) images with different magnifications (Fig. S4†) showed that both MsH-MPF-H_2 and MsH-MPF-H_2O nanospheres had an average particle size of ~70 nm and displayed mesopores on the rough surface. To confirm the effect of P-123 on the design of the interior structure, mesofree-MPF was synthesized without P-123 as the soft template. As expected, the TEM image of mesofree-MPF exhibited nanospheres without interior configuration (Fig. S5†). The electron microscopy analyses verified the mesoporous multi-shelled configuration of both MsH-MPF-H_2 and MsH-MPF-H_2O. Besides, the periodic interfaces due to multiple shells were confirmed by SAXS as shown in Fig. S6.† The SAXS patterns of both MsH-MPF-H_2 and MsH-MPF-H_2O exhibited two broad peaks, corresponding to the periodic fluctuation of internal electron density caused by unique periodic interfaces. The above analyses revealed the multi-shelled structure of the material and its accompanying periodic interface from several characterization techniques.

Furthermore, the mesopores and hollow interior nanostructure were investigated by nitrogen sorption analyses and energy-dispersive spectroscopy (EDS) line scanning. Firstly, the nitrogen sorption isotherm of MsH-MPF-H_2 showed a typical type-H1 isotherm and the corresponding cumulative pore volume was 0.78 $cm^3\ g^{-1}$, demonstrating abundant mesopores in MsH-MPF-H_2. According to the Barrett–Joyner–Halenda (BJH) method, MsH-MPF-H_2 nanospheres contained mesopores centered at 4.2 nm and 3.5 nm (Fig. 2b), which were derived from the presence of mesopores on resin shells. A broad peak at 50 nm was also observed, indicating multi-shelled hollow nanospheres. MsH-MPF-H_2O exhibited similar N_2 sorption isotherms to MsH-MPF-H_2 and a pore volume of 0.71 $cm^3\ g^{-1}$ (Fig. S7 and S8†), revealing similar porosity of the two samples. The consistent pore structure of MsH-MPF nanospheres derived from different pyrolysis atmospheres, which was beneficial to clarifying the effect of atomic structures. Meanwhile for mesofree-MPF, there was almost no mesopore in mesofree-MPF, and the cumulative pore volume of mesofree-MPF was 0.15 $cm^3\ g^{-1}$. The absence of a pore structure in mesofree-MPF suggests that P-123 is responsible for the interior structure of MsH-MPF-H_2 and MsH-MPF-H_2O. Moreover, the pore structure of MsH-MPF-H_2 was checked by performing element line scanning (Fig. 2c and d). The distribution of nitrogen element for MsH-MPF-H_2 fluctuated obviously with the change of the position. Two depressions with a width of 5 nm and 3.9 nm, respectively, represented the typical mesoporous structure of MsH-MPF-H_2. The fluctuations of carbon element were not obvious, because the distribution of carbon element was affected by the process of collecting the mapping of elements. The above analyses had demonstrated the nanostructure of MsH-MPF-H_2 from different perspectives, indicating the simultaneous integration of multiple mesoporous shells and hollow characteristics.

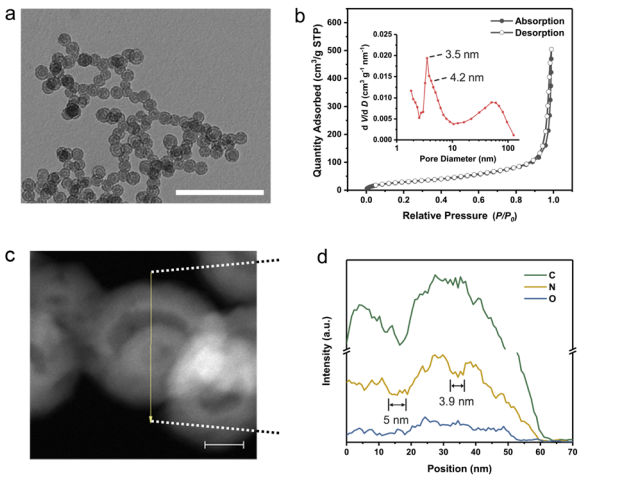

Fig. 2 Morphology and porosity characterization. (a) TEM image for MsH-MPF-H_2 nanospheres with a scale bar of 500 nm. (b) N_2 absorption–desorption isotherm of MsH-MPF-H_2 nanospheres and inset shows the corresponding pore size distribution curve. d*V*/d*D*, differential pore volume distribution; *V*, pore volume; *D*, pore diameter. (c) Dark-field image for MsH-MPF-H_2 nanospheres with a scale bar of 20 nm. (d) Energy-dispersive spectrometer (EDS) line–scan profile of MsH-MPF-H_2 nanospheres as shown in (c).

Atomic structure analysis

The atomic configuration of MsH-MPF-H_2 was clarified by using X-ray absorption near-edge spectroscopy (XANES) analysis and FT-IR spectra, indicating a weak hydrogen bond of MsH-MPF-H_2. As shown in C K-edge XANES spectra (Fig. 3a), two typical spectroscopic features of $\pi^*_{\text{OH-substituted benzene}}$ (287.2 eV) and $\sigma^*_{\text{C–OH}}$ (289.2 eV) represented possible species to form hydrogen bonds.[27,28] MsH-MPF-H_2 exhibited a weak peak at 287.2 eV, attributed to OH-substituted benzene. In particular, the absence of the peak at 289.2 eV in MsH-MPF-H_2 indicated that there was no alcoholic hydroxyl coordination. The XANES results confirmed that the content of hydroxyl, a possible hydrogen-bonding species, was lower in MsH-MPF-H_2 compared with MsH-MPF-H_2O. The XANES results revealed that the hydroxyl branches in MsH-MPF-H_2 were controlled *via* H_2-rich argon assistance. Moreover, the FT-IR spectra showed that the hydrogen bond strength of MSH-MPF-H_2 was relatively weak than that of MsH-MPF-H_2O. As shown in Fig. 3b, the bands at 1571 cm^{-1} corresponding to the vibration of the benzene ring[29] were almost coincident for both MsH-MPF-H_2 and MsH-MPF-H_2O, indicating that the carbon skeleton structure barely changed with different pyrolysis atmospheres. Therefore this band was set as the benchmark for further analysis. The broad

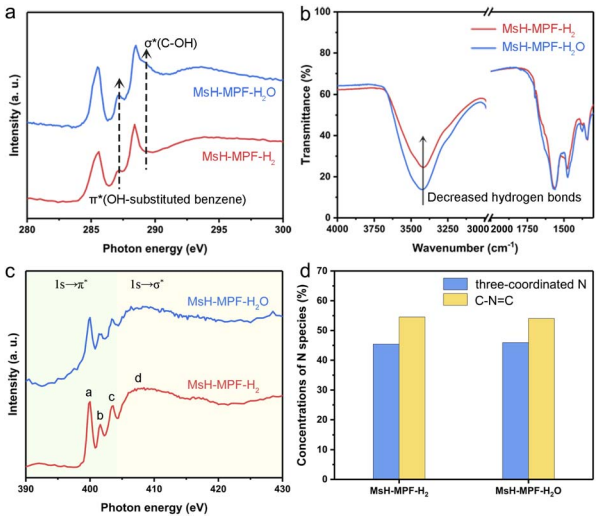

Fig. 3 Atomic structure analysis. (a) Carbon and (c) nitrogen K-edge X-ray absorption near-edge spectroscopy (XANES) of MsH-MPF-H_2 and MsH-MPF-H_2O nanospheres, respectively. (b) FT-IR spectra of MsH-MPF-H_2 and MsH-MPF-H_2O nanospheres, respectively. (d) Concentrations of N species in MsH-MPF-H_2 and MsH-MPF-H_2O according to the X-ray photoelectron spectroscopy (XPS) spectrum.

band observed at around 3400 cm^{-1} was linked to –OH stretching, and the intensity significantly decreased in MsH-MPF-H_2, indicating the broken hydrogen bond with the assistance of H_2-rich argon.[30,31] Overall, MsH-MPF-H_2 nanospheres exhibited the characteristics of poor hydrogen bond.

To assess the effect of H_2O on MsH-MPF-H_2O, X-ray photoelectron spectroscopic (XPS) analysis of carbon element for MsH-MPF-H_2O at different temperatures was performed. As shown in Fig. S9,† the high-resolution spectrum of C 1s is divided to three main peaks corresponding to C–C, C=N, and C–O/N species and a minor peak for C=O at temperatures including 298 K, 373 K and 423 K.[32] The C 1s spectra of the MsH-MPF-H_2O sample did not show significant changes at all temperatures tested. Meanwhile, the relative surface concentrations of different carbon species remained consistent at all temperatures tested, illustrating that the robust atomic structure of MSH-MPF-H_2O was not affected by adsorbed water.

To evaluate the chemical composition and valence states of MsH-MPF-H_2 and MsH-MPF-H_2O, their nitrogen K-edge XANES spectra have been recorded. As shown in Fig. 3c, the nitrogen K-edge of both MsH-MPF-H_2 and MsH-MPF-H_2O presents similar four obvious resonances, due to π* transition of the N atoms of triazine (peak a) and the pyramidal three-coordinated N atoms adjacent to the sp^2 C atoms of triazine (peaks b and c), and σ* transition of the C–N bond (peak d).[33] The above results can be further demonstrated by the XPS spectra of N element. As shown in Fig. S10,† the high-resolution spectrum of N 1s of both MsH-MPF-H_2 and MsH-MPF-H_2O exhibits two main peaks corresponding to pyramidal three-coordinated N and C–N=C (N atoms of triazine).[34] The relative surface concentrations of N species in MsH-MPF-H_2 and MsH-MPF-H_2O were consistent (Fig. 3d). The above analysis indicated that the bonding states of nitrogen element in MsH-MPF-H_2 and MsH-MPF-H_2O were basically the same.

Thermal performance

MsH-MPF-H_2 nanospheres with abundant mesopores and periodic interfaces provide the feasibility to achieve the minimum limit of thermal conductivity. Laser flash apparatus (LFA) measurement was performed to determine the temperature dependent thermal conductivity of MsH-MPF-H_2 nanospheres (Fig. 4a). MsH-MPF-H_2 realized an ultralow thermal conductivity of 0.013 W m^{-1} K^{-1} at 298 K. Intriguingly, the thermal conductivity of MsH-MPF-H_2 remained relatively stable as temperature rises, which was different from the monotonously increasing thermal conductivity of silica aerogel, a typical thermal insulator.[35] Even at 473 K, thermal transport in MsH-MPF-H_2 kept suppressed, and the thermal conductivity was maintained at 0.013 W m^{-1} K^{-1}. MsH-MPF-H_2 nanospheres achieved ultralow thermal conductivity, indicating its superiority in thermal insulation. To intuitively clarify the impact of the mesoporous multi-shelled hollow nanostructure and weak hydrogen bond on ultralow thermal conductivity, the thermal properties of different samples were assessed. As shown in Fig. 4b, the thermal conductivity of mesofree-MPF was 1.8 times that of MsH-MPF-H_2 at 298 K and remained higher than that of MsH-MPF-H_2 from 298 K to 473 K (Fig. S11†). Meanwhile MsH-MPF-H_2O exhibited slightly higher thermal conductivity than MsH-MPF-H_2. These results revealed that the mesoporous multi-shelled hollow nanostructure played a vital role in inhibiting heat convection, while a poor H-bond further restricted heat conduction and the complementary strategy drove the thermal conductivity of MsH-MPF to the minimum limit.

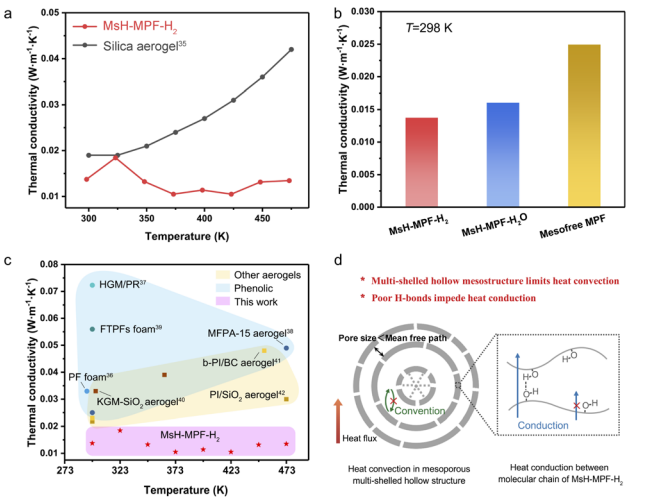

Fig. 4 Thermal performance. (a) Thermal conductivity of MsH-MPF-H_2 nanospheres by LFA measurement and thermal conductivity of silica aerogel from the literature.[35] (b) Thermal conductivity of MsH-MPF-H_2, MsH-MPF-H_2O and mesofree-MPF at 298 K from LFA measurement. (c) Thermal conductivity comparison between MsH-MPF-H_2 nanospheres and typical thermal insulating polymer materials in the literature.[36–42] (d) Schematic illustration for suppression of thermal transport in MsH-MPF-H_2.

Benefitting from the ingenious mesoporous multi-shelled hollow nanostructure, MsH-MPF-H_2 exhibited ultralow thermal conductivity. To compare the thermal insulation performance of MsH-MPF-H_2 with different kinds of typical thermal insulating material, thermal conductivity was selected as an indicator. As shown in Fig. 4c, the thermal conductivity of phenolic resin-based materials ranged from 0.02 W m^{-1} K^{-1} to 0.08 W m^{-1} K^{-1}.[36–39] Meanwhile for materials based on other polymers such as polyimide, the thermal conductivity ranged from 0.02 W m^{-1} K^{-1} to 0.05 W m^{-1} K^{-1}.[40–42] In general, few materials could achieve thermal conductivity below 0.02 W m^{-1} K^{-1}. Nevertheless, due to the mesoporous multi-shelled hollow nanostructure and broken hydrogen bonds, MsH-MPF-H_2 nanospheres exhibited lower than 0.02 W m^{-1} K^{-1} thermal conductivity from 298 to 473 K, which was rarely observed in other insulating materials. MsH-MPF-H_2 nanospheres performed better than other thermal insulating materials in a wide temperature range, indicating the importance of precise design of mesoporous multi-shelled hollow nanostructures.

The ultralow thermal conductivity of MsH-MPF-H_2 nanospheres was attributed to the gas-boundary scattering caused by abundant mesopores and periodic interfaces. As shown in Fig. 4d, the thickness of hollow layers is much less than the molecular mean free path of air (about 70 nm), and thus the boundary scattering of gas molecules becomes significant, effectively suppressing heat convection.[43–45] The broken hydrogen bond leads to further thermal conductivity reduction, since the transport of phonons is disturbed.[46,47] Benefiting from the precise interior nanoscale design, the thermal conductivity of MsH-MPF-H_2 nanospheres is propelled to the minimum boundary accordingly.

Conclusions

In conclusion, we demonstrated a mesoporous multi-shelled hollow nanostructure by an *in situ* polymerization strategy, achieving ultralow thermal conductivity. The elaborate interior nanostructure of the adiabatic monomer is realized through the immobilization of the multi-shelled vesicle structure of the soft template by *in situ* polymerization. Benefiting from abundant mesopores and periodic interfaces, heat convection is significantly suppressed. Consequently, the thermal conductivity of MsH-MPF-H_2 reaches down to 0.013 W m^{-1} K^{-1} at 298 K and shows unusual stability from 298 K to 473 K. We anticipate that the *in situ* polymerization strategy provides a new approach for the construction of a hollow nanostructure with mesoporous multiple shells and contribute to producing functionalized nanomaterials for potential applications.

Experimental

Synthesis of MsH-MPF-H_2 and MsH-MPF-H_2O nanospheres

In a typical synthesis, 2.4 g melamine, 560 μL phenol, and 15 mL NaOH aqueous solution (0.1 mol L^{-1}) were mixed and heated to 50 °C. Then 3.8 mL formaldehyde was added, followed by heating at 70 °C for 30 min until the solution became transparent. 15 mL P-123 solution (0.064 g mL^{-1}) was added to the transparent solution, and the mixture was stirred at 66 °C for 2 h. Subsequently, 50 mL deionized water was poured into the solution under stirring at 70 °C for 10 hours. Then, the 4.5 mL solution synthesized above was dispersed in 27.5 mL deionized water, and the mixed solution was transferred into a Teflon-lined autoclave and heated at 120 °C for 24 h. The precursor was centrifuged and washed with deionized water, followed by freeze-drying. To obtain MsH-MPF-H_2, the precursor was pyrolysis in a tubular furnace under 5% H_2 with a 95% argon atmosphere in 320 °C for 1 hour with a heating rate of 1 °C min^{-1}. MsH-MPF-H_2O was obtained under an H_2O-rich argon atmosphere *via* the same temperature program as MsH-MPF-H_2.

Synthesis of mesofree-MPF nanospheres

Mesofree-MPF was synthesized similarly to MsH-MPF-H_2. Briefly, P-123 solution was replaced with 15 mL of distilled water. After the same process, 32 mL obtained solution was transferred into a Teflon-lined autoclave without attenuation and heated at 120 °C for 24 h. The precursor that had been cleaned and dried was pyrolysed *via* the same atmosphere and temperature as MsH-MPF-H_2.

Measurements of thermal conductivity at different temperatures

The thermal conductivity (κ) of all samples was investigated with a diameter of 8 mm in ambient air at 298–473 K. The κ was calculated by using the equation

$$\kappa = \alpha \rho C_P$$

where α is the measured thermal conductivity, ρ is the calculated density, and C_P is the measured specific heat capacity.

Characterization

The pyrolysis process was analyzed by a combination of a thermogravimeter (PerkinElmer, Pyris 1) and Fourier transform infrared spectrometer (PerkinElmer, Frontier). Fourier transform infrared (FT-IR) spectroscopy was carried out on a Nicolet 8700 FT-IR. C and N K-edge sXAS spectra were recorded at the beamline MCD of National Synchrotron Radiation Laboratory (NSRL, Hefei) in the total electron yield (TEY) mode by collecting the sample drain current under a vacuum better than 10^{-7} Pa. X-ray photoelectron spectroscopy (XPS) characterization was performed on an ESCALAB MK II with the excitation source of Mg Kα = 1253.6 eV. The transmission electron microscopy (TEM) images were obtained by using a H-7700 (Hitachi, Japan) operated at an acceleration voltage of 100 kV. The scanning electron microscopy (SEM) image was taken on a HITACHI SU8220 SEM. Small-angle X-ray Scattering (SAXS) measurements were carried out by using an Anton Paar SAXSpoint 2.0 using an X-ray source with a Cu target. The nitrogen sorption isotherms were recorded using a Micromeritics ASAP 2000 system at 77 K (λ = 1.5412 Å). High resolution TEM (HRTEM) images and corresponding energy dispersive spectroscopy (EDS) mapping analyses were performed on a JEM-2100F field-

emission electron microscope operated at an acceleration voltage of 200 kV. The thermal conductivity of different samples was analyzed by using a Laser Flash Apparatus (LFA467, Netzsch, Germany).

Data availability

All data supporting this study are available in the manuscript and ESI.†

Author contributions

Ruilin Yuan performed the experiments and measurements, analyzed the characterizations, and prepared the manuscript. Chun Wang assisted in thermal conductivity measurements. Long Chen contributed to the systhensis. Han Cheng and Wentuan Bi gave suggestions to the manuscript. Wensheng Yan conducted the Synchrotron-based X-ray absorption near-edge spectroscopy experiments. Yi Xie supervised the project. Changzheng Wu held the project and edited the paper. All the authors contributed to the overall scientific interpretation and approved the final version of the manuscript.

Conflicts of interest

There are no conflicts to declare.

Acknowledgements

This work was financially supported by the National Basic Research Program of China (No. 2017YFA0206702), the Natural Science Foundation of China (No. 21925110, 21890750, and 22175051), the Users with Excellence Project of Hefei Science Center, CAS (2021HSC-UE004), the Strategic Priority Research Program of the Chinese Academy of Sciences (No. XDB36000000),
CAS Project for Young Scientists in Basic Research, Grant No.YSBR-070, Key Research & Development Plan of Shandong Province (2021CXGC010302), and the China National Postdoctoral Program for Innovative Talents (BX2021283). The authors appreciate the beamlines MCD-A and MCD-B at the National Synchrotron Radiation Laboratory (NSRL).

Notes and references

1 X. Wang, J. Feng, Y. Bai, Q. Zhang and Y. Yin, *Chem. Rev.*, 2016, **116**, 10983–11060.
2 L. Yu, X. Y. Yu and X. W. Lou, *Adv. Mater.*, 2018, **30**, 1800939.
3 J. Zhang, L. Yu, Y. Chen, X. F. Lu, S. Gao and X. W. Lou, *Adv. Mater.*, 2020, **32**, 1906432.
4 Y. Z. Wang, M. Yang, Y. M. Ding, N. W. Li and L. Yu, *Adv. Funct. Mater.*, 2022, **32**, 2108681.
5 C. Wu, X. Zhang, B. Ning, J. Yang and Y. Xie, *Inorg. Chem.*, 2009, **48**, 6044–6054.
6 R. Bi, N. Xu, H. Ren, N. Yang, Y. Sun, A. Cao, R. Yu and D. Wang, *Angew. Chem., Int. Ed.*, 2020, **59**, 4865–4868.
7 D. Gu, H. Bongard, Y. Deng, D. Feng, Z. Wu, Y. Fang, J. Mao, B. Tu, F. Schuth and D. Zhao, *Adv. Mater.*, 2010, **22**, 833–837.
8 X. Lai, J. Li, B. A. Korgel, Z. Dong, Z. Li, F. Su, J. Du and D. Wang, *Angew. Chem., Int. Ed. Engl.*, 2011, **50**, 2738–2741.
9 H.-J. Zhan, K.-J. Wu, Y.-L. Hu, J.-W. Liu, H. Li, X. Guo, J. Xu, Y. Yang, Z.-L. Yu and H.-L. Gao, *Chem*, 2019, **5**, 1871–1882.
10 W. Xiao, J. Zhou, L. Yu, D. Wang and X. W. Lou, *Angew. Chem., Int. Ed.*, 2016, **55**, 7427–7431.
11 R. Zeng, K. Lian, B. Su, L. Lu, J. Lin, D. Tang, S. Lin and X. Wang, *Angew. Chem., Int. Ed.*, 2021, **60**, 25055–25062.
12 J. Yu, J. Xiao, A. Li, Z. Yang, L. Zeng, Q. Zhang, Y. Zhu and L. Guo, *Angew. Chem., Int. Ed.*, 2020, **59**, 13071–13078.
13 L. Han, P. Xiong, J. Bai and S. Che, *J. Am. Chem. Soc.*, 2011, **133**, 6106–6109.
14 M. Feyen, C. Weidenthaler, F. Schüth and A.-H. Lu, *J. Am. Chem. Soc.*, 2010, **132**, 6791–6799.
15 E. González, J. Arbiol and V. F. Puntes, *Science*, 2011, **334**, 1377–1380.
16 L. Peng, H. Peng, Y. Liu, X. Wang, C.-T. Hung, Z. Zhao, G. Chen, W. Li, L. Mai and D. Zhao, *Sci. Adv.*, 2021, **7**, eabi7403.
17 J. Liu, T. Yang, D.-W. Wang, G. Q. Lu, D. Zhao and S. Z. Qiao, *Nat. Commun.*, 2013, **4**, 2798–2805.
18 Z. Teng, X. Su, Y. Zheng, J. Zhang, Y. Liu, S. Wang, J. Wu, G. Chen, J. Wang, D. Zhao and G. Lu, *J. Am. Chem. Soc.*, 2015, **137**, 7935–7944.
19 G. Zhou, Y. Chen, J. Yang and S. Yang, *J. Mater. Chem.*, 2007, **17**, 2839–2844.
20 T. Shimizu, M. Masuda and H. Minamikawa, *Chem. Rev.*, 2005, **105**, 1401–1444.
21 Y. Zhang, M. Yu, L. Zhou, X. Zhou, Q. Zhao, H. Li and C. Yu, *Chem. Mater.*, 2008, **20**, 6238–6243.
22 K. Wang, L. Yang, H. Li and F. Zhang, *ACS Appl. Mater. Interfaces*, 2019, **11**, 21815–21821.
23 C. Devallencourt, J. Saiter, A. Fafet and E. Ubrich, *Thermochim. Acta*, 1995, **259**, 143–151.
24 F.-D. Kopinke, M. Remmler, K. Mackenzie, M. Möder and O. Wachsen, *Polym. Degrad. Stab.*, 1996, **53**, 329–342.
25 F. Bérubé and S. Kaliaguine, *Microporous Mesoporous Mater.*, 2008, **115**, 469–479.
26 K. A. Trick and T. E. Saliba, *Carbon*, 1995, **33**, 1509–1515.
27 Y. Zubavichus, A. Shaporenko, M. Grunze and M. Zharnikov, *J. Phys. Chem. A*, 2005, **109**, 6998–7000.
28 J. Zhong, H. Zhang, X. Sun and S. T. Lee, *Adv. Mater.*, 2014, **26**, 7786–7806.
29 J. H. Lee, H. J. Lee, S. Y. Lim, B. G. Kim and J. W. Choi, *J. Am. Chem. Soc.*, 2015, **137**, 7210–7216.
30 L. Song, T. Zhu, L. Yuan, J. Zhou, Y. Zhang, Z. Wang and C. Tang, *Nat. Commun.*, 2019, **10**, 1315–1323.
31 P. F. Cao, B. Li, T. Hong, J. Townsend, Z. Qiang, K. Xing, K. D. Vogiatzis, Y. Wang, J. W. Mays, A. P. Sokolov and T. Saito, *Adv. Funct. Mater.*, 2018, **28**, 1800741.
32 A. Dementjev, A. De Graaf, M. Van de Sanden, K. Maslakov, A. Naumkin and A. Serov, *Diamond Relat. Mater.*, 2000, **9**, 1904–1907.
33 O. Plashkevych, A. Snis, L. Yang, H. Ågren and S. Matar, *Phys. Scr.*, 2001, **63**, 70–86.

34 D. Feng, Z. Zhou and M. Bo, *Polym. Degrad. Stab.*, 1995, **50**, 65–70.
35 G. Wei, Y. Liu, X. Zhang, F. Yu and X. Du, *Int. J. Heat Mass Transfer*, 2011, **54**, 2355–2366.
36 F. Song, Z. Li, P. Jia, C. Bo, M. Zhang, L. Hu and Y. Zhou, *Mater. Des.*, 2020, **192**, 108668.
37 H. Yang, Y. Jiang, H. Liu, D. Xie, C. Wan, H. Pan and S. Jiang, *J. Colloid Interface Sci.*, 2018, **530**, 163–170.
38 K. Wu, W. Dong, Y. Pan, J. Cao, Y. Zhang and D. Long, *Ind. Eng. Chem. Res.*, 2021, **60**, 1241–1249.
39 J. Liu, L. Wang, W. Zhang and Y. Han, *Materials*, 2020, **13**, 148.
40 J. Zhu, J. Hu, C. Jiang, S. Liu and Y. Li, *Carbohydr. Polym.*, 2019, **207**, 246–255.
41 X. Zhang, X. Zhao, T. Xue, F. Yang, W. Fan and T. Liu, *Chem. Eng. J.*, 2020, **385**, 123963.
42 W. Fan, X. Zhang, Y. Zhang, Y. Zhang and T. Liu, *Compos. Sci. Technol.*, 2019, **173**, 47–52.
43 Z. L. Yu, N. Yang, V. Apostolopoulou-Kalkavoura, B. Qin, Z. Y. Ma, W. Y. Xing, C. Qiao, L. Bergström, M. Antonietti and S. H. Yu, *Angew. Chem., Int. Ed.*, 2018, **57**, 4538–4542.
44 B. Wicklein, A. Kocjan, G. Salazar-Alvarez, F. Carosio, G. Camino, M. Antonietti and L. Bergström, *Nat. Nanotechnol.*, 2015, **10**, 277–283.
45 Y. Cui, H. Gong, Y. Wang, D. Li and H. Bai, *Adv. Mater.*, 2018, **30**, 1706807.
46 G.-H. Kim, D. Lee, A. Shanker, L. Shao, M. S. Kwon, D. Gidley, J. Kim and K. P. Pipe, *Nat. Mater.*, 2015, **14**, 295–300.
47 L. Zhang, M. Ruesch, X. Zhang, Z. Bai and L. Liu, *RSC Adv.*, 2015, **5**, 87981–87986.